

CHAPTER 2

TETRANUCLEAR IRON CLUSTERS WITH A VARIED INTERSTITIAL LIGAND:
EFFECTS ON STRUCTURE, REDOX PROPERTIES, AND NITRIC OXIDE
ACTIVATION

The text for this chapter was reproduced in part from:

Reed, C. J.; Agapie, T. *Inorg. Chem.*, **2017**, *56*, 13360-13367

ABSTRACT

A new series of tetranuclear Fe clusters displaying an interstitial μ_4 -F ligand was prepared for a comparison to previously reported μ_4 -O analogues. With a single nitric oxide (NO) coordinated as a reporter of small-molecule activation, the μ_4 -F clusters were characterized in five redox states, from $\text{Fe}^{\text{II}}_3\{\text{FeNO}\}^8$ to $\text{Fe}^{\text{III}}_3\{\text{FeNO}\}^7$, with NO stretching frequencies ranging from 1680 to 1855 cm^{-1} , respectively. Despite accessing more reduced states with an F^- bridge, a two-electron reduction of the distal Fe centers is necessary for the μ_4 -F clusters to activate NO to the same degree as the μ_4 -O system; consequently, NO reactivity is observed at more positive potentials with μ_4 -O than μ_4 -F. Moreover, the μ_4 -O ligand better translates redox changes of remote metal centers to diatomic ligand activation. The implication for biological active sites is that the higher-charge bridging ligand is more effective in tuning cluster properties, including the involvement of remote metal centers, for small-molecule activation.

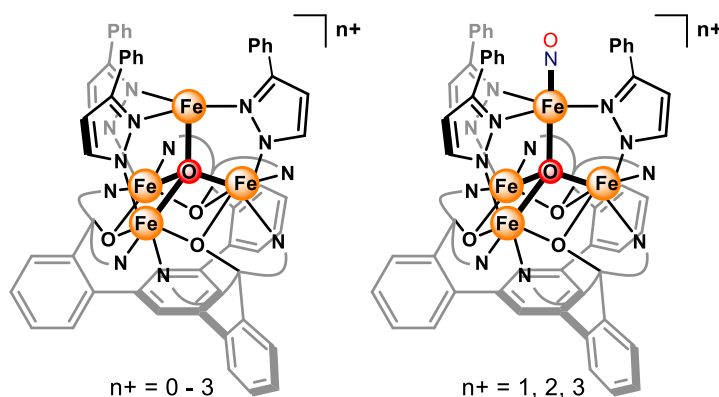
INTRODUCTION

Transition metal clusters perform diverse functions in proteins, including metal storage, sensing, electron transfer, and multi-electron small molecule conversions (such as H₂O oxidation, CO₂ fixation, and N₂ reduction).¹ A common element of these multinuclear sites is the presence of highly bridged ($\geq \mu_3$ -binding) single atom ligands, such as sulfide,² oxide,³ or carbide.⁴ Quantitative measures of the effects these ligands play in small molecule activation remain rare. This is particularly relevant to understanding the role the interstitial μ_6 -C ligand in the FeMo cofactor (FeMoco) of nitrogenase (Figure 1A). Synthetic clusters suitable for structure-function studies of bridging ligands with respect to the activation of a small molecule are rare, likely because of design constraints that are difficult to overcome by self-assembly, which is the route typically employed in cluster synthesis. Maintaining the exact same structure while changing the bridging ligands and redox states while limiting ligand binding to a single small molecule, desirable for quantification of the effect and for mimicking substrate activation by protein active sites, are two major challenges. A host of iron carbonyl clusters have been synthesized with a variety of bridging ($\geq \mu_3$) single-atom ligands, including μ_6 -C clusters, such as $[(\mu_6\text{-C})\text{Fe}_6(\text{CO})_{16}]^{2-}$, with arrangements reminiscent of the FeMoco structure (Figure 1B).⁵ While a related cluster has been reported displaying a μ_6 -N ligand, $[(\mu_6\text{-N})\text{Fe}_6(\text{CO})_{15}]^{3-}$ has been reported, with potential for structure-function studies of the effect of the interstitial ligand, changes in the structure and number of carbon monoxide (CO) ligands complicate interpretations. In the cases where completely isostructural clusters can be prepared with bridging elements of the second row of the periodic table, the large number (≥ 9) of diatomic ligands limits interpretations regarding the activation of a *single* small molecule substrate, which is most relevant to biological systems. Recently, in an elegant demonstration of the effect of the μ_4 -ligand (N vs C) on reactivity, the hydride ligands in $[\text{HFe}_4\text{C}(\text{CO})_{12}]^{2-}$ and $[\text{HFe}_4\text{N}(\text{CO})_{12}]^{-}$

have been shown to have distinct behavior for H₂ and formate generation.⁶ Other synthetic clusters have been studied to address effects of a bridging ligand on reduction potentials or to model FeMoco, but small molecule binding by the clusters with different bridging ligands has not been reported.⁷

Toward directly interrogating the effect of a cluster's interstitial ligand on reactivity, we have developed synthetic methodologies to access site-differentiated multinuclear complexes that allow variation of the bridging ligands. Initial studies by Dr. Graham de Ruiter established a synthetic route to tetranuclear Fe clusters arranged in a pseudo-tetrahedral geometry around a μ_4 -O ligand. One of these Fe centers displays a trigonal pyramidal coordination geometry, with an open coordination site *trans* to the μ_4 -O and the three neighboring Fe centers; this open coordination site is facilitated by steric protection of phenyl-pyrazolate ligands, which preclude binding of most ligands except for small molecules. These clusters, **LFe₃O(PhPz)₃Feⁿ⁺**, were competent to bind and activate nitric oxide (NO; Scheme 1), where redox changes of the distal Fe centers were able to modulate the degree of NO activation and reactivity.⁸ In summary, reduction of a distal Fe^{III} to Fe^{II} leads to an average decrease of N–O stretching frequency of $\sim 50 - 30 \text{ cm}^{-1}$, where the lowest oxidation state NO cluster observed (Fe^{II}₂Fe^{III}{FeNO})⁷ displayed reactivity towards NO disproportionation.

Scheme 1. Related Tetranuclear Clusters Previously Reported by the Agapie Group⁸



Herein, we present investigations of a series of tetranuclear iron clusters containing a μ_4 -F motif, isostructural with the previously reported μ_4 -O clusters (Figure 1C).^{8,9} These compounds allow for the evaluation of the effects of the nature of the interstitial atom on cluster properties related to the activation of a single diatomic ligand (NO).

RESULTS AND DISCUSSION

We have recently reported the synthesis of site differentiated tetranuclear clusters, where three (basal) metal centers are coordinated by a hexapyridyl trialkoxide framework (\mathbf{L}^3 , Figure 1C) and bridged to a fourth (apical) metal site through three pyrazolate ligands and a μ_4 -O ligand.^{8,9} The all-ferrous fluoride-bridged cluster, **1**, was synthesized via addition of a 2:1 ratio of phenylpyrazole and potassium phenylpyrazolate along with 1 equiv of anhydrous tetrabutylammonium fluoride to a previously reported trinuclear iron precursor ($\mathbf{LFe}_3(\text{OAc})(\text{OTf})_2$; Figure 1C).^{8,10} The fourth Fe equivalent was delivered as $\text{Fe}(\text{N}(\text{SiMe}_3)_2)_2$ to complete the tetranuclear cluster (**1**). This redox-neutral route of installing the interstitial F proved to be the most reliable way to avoid the generation of mixtures of clusters, with some μ_4 -O clusters likely having formed due to trace moisture. Subsequent chemical oxidations afford two additional redox states, $[\text{Fe}^{\text{II}}_3\text{Fe}^{\text{III}}]$ (**2**) and $[\text{Fe}^{\text{II}}_2\text{Fe}^{\text{III}}_2]$ (**3**); cyclic voltammetry of **1** displays two quasi-reversible features for these oxidations at potentials of -0.51 V (all potentials vs Fc/Fc^+) and +0.18 V (Figure 2). Characterization by Mössbauer spectroscopy is consistent with charge localization on each Fe center and with oxidations occurring exclusively in the basal triiron core, the apical Fe remaining Fe^{II} (Figure 3), as was observed for the μ_4 -O analogs.^{9a} Structural characterization by single crystal X-ray diffraction (XRD) reveals that the most oxidized cluster, **3**, displays a five-coordinate apical Fe^{II} , due to acetonitrile (MeCN) binding (Figure 4). Removal of this ligand under vacuum results in decomposition. This behavior is in contrast to the analogous μ_4 -O clusters, which have been isolated in the

$[\text{Fe}^{\text{II}}_2\text{Fe}^{\text{III}}_2]$ and $[\text{Fe}^{\text{II}}\text{Fe}^{\text{III}}_3]$ oxidation states, both displaying a four-coordinate apical Fe^{II} . This difference suggests that that the $\mu_4\text{-F}$ clusters are more Lewis acidic than their $\mu_4\text{-O}$ analogues. Consistent with this interpretation, $\mu_4\text{-O}$ clusters with electron withdrawing substituents show increased coordination numbers at the apical metal.^{9a}

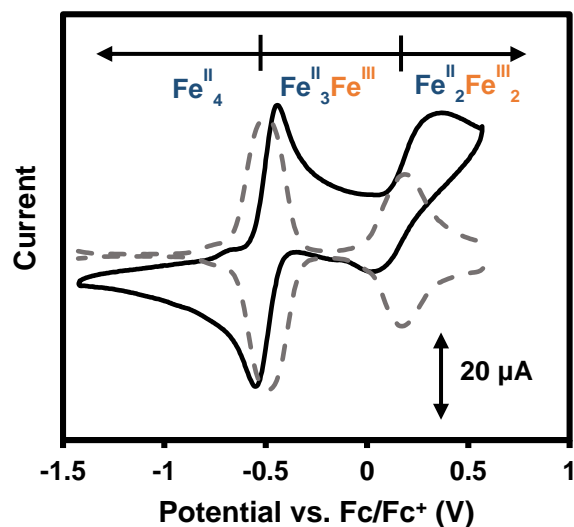


Figure 2. Cyclic voltammogram (black trace) of **1** (3 mM) in MeCN with 85 mM $[\text{Bu}_4\text{N}][\text{PF}_6]$ at a scan rate of 200 mV/s with glassy carbon, Pt-wire, and Ag-wire as working, counter, and reference electrode, respectively. Square wave voltammograms (gray dashed trace) overlaid with 0.1 V amplitude, 1.0 s period, and 0.01 V increment.

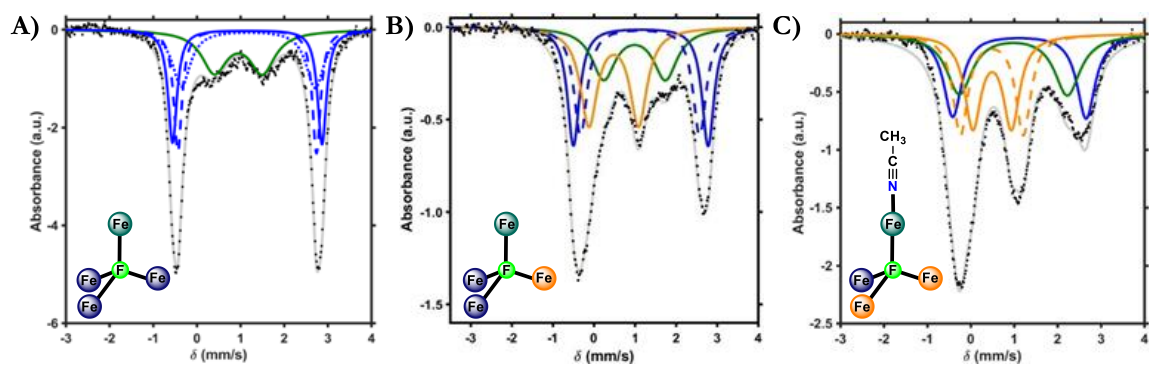


Figure 3. ^{57}Fe Mössbauer spectra at 80K of (A) **1**, (B) **2**, and (C) **3**. Black dots represent the data, gray traces are the sum of the simulated fits, and colored traces represent the individual fits for the Fe centers (See Table 1 for parameters). Blue traces represent assignments made to basal Fe^{II} , orange traces represent basal Fe^{III} assignments, green traces represent apical Fe^{II} .

Table 1. ^{57}Fe Mössbauer Parameters for Complexes **1** – **3** with Oxidation State Assignments

	δ (mm/s)	$ \Delta E_q $ (mm/s)	%	assignment
1				
—	1.16	3.42	25	<i>h.s.</i> Fe^{II}
- - -	1.15	3.18	25	<i>h.s.</i> Fe^{II}
⋯	1.18	3.07	25	<i>h.s.</i> Fe^{II}
—	0.95	1.10	25	<i>h.s.</i> Fe^{II}
2				
—	1.14	3.30	25	<i>h.s.</i> Fe^{II}
- - -	1.12	2.90	25	<i>h.s.</i> Fe^{II}
—	0.48	1.21	29	<i>h.s.</i> Fe^{III}
—	0.99	1.50	21	<i>h.s.</i> Fe^{II}
3				
—	1.12	3.07	25	<i>h.s.</i> Fe^{II}
—	0.49	0.89	25	<i>h.s.</i> Fe^{III}
- - -	0.49	1.45	25	<i>h.s.</i> Fe^{III}
—	0.98	2.49	25	<i>h.s.</i> Fe^{II}

NO provides a diagnostic vibrational spectroscopic signature for comparing different complexes to address the effects of the multinuclear supporting platform and the interstitial ligand on small-molecule binding.¹¹ Studies of the chemistry of Fe clusters with NO have been

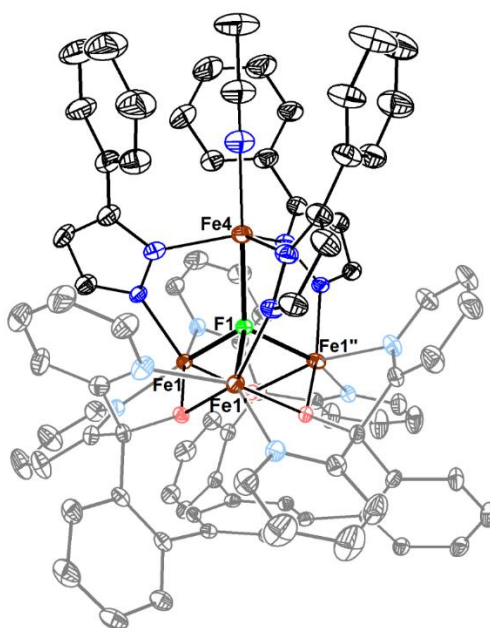


Figure 4. Crystal structure of **3**. Ellipsoids are shown at the 50% probability level. Hydrogen atoms, solvent molecules, and outersphere counterions omitted for clarity.

principally focused on understanding the biologically relevant conversion of Fe–S clusters to nitrosylated products.¹² However, there are few examples of multinuclear mononitrosyl complexes containing nearby redox-active metal centers.^{8,13} The clusters targeted here provide insight into the influence of neighboring metal centers on the chemistry of the metal nitrosyl moiety. The addition of NO to compound **1** leads to the formation of the corresponding nitrosyl adduct. Cyclic voltammetry of the monocationic nitrosyl cluster, **1-NO**, displays three electrochemically quasi-reversible oxidations and one quasi-reversible reduction (Figure 5). Each of the five redox states of the nitrosyl clusters observed electrochemically was accessed synthetically (Figure 1C). Stepwise treatment of **1-NO** with AgOTf (**2-NO** and **3-NO**) and [(2,4-Br-C₆H₄)₃N][SbCl₆] (**4-NO**) provides access to the oxidized NO adducts. **4-NO** decomposes in solution and as a solid on the time scale of attempted crystallizations, preventing structural characterization. Reduction of **1-NO** with decamethylcobaltocene in

MeCN precipitates a purple solid assigned as **5-NO**. Dissolution of **5-NO** in tetrahydrofuran, pyridine, or dichloromethane (CH_2Cl_2), leads to rapid decomposition, preventing structural characterization of this complex as well (Figure 6). Reoxidation of a MeCN suspension of **5-NO** with silver triflate (AgOTf) leads to isolation of the one electron oxidized cluster, **1-NO**, in good yield (Figure 7). Nitrous oxide (N_2O) is detected upon decomposition of **5-NO**, albeit in low yield (~ 0.1 equiv, gas chromatography-mass spectrometry).

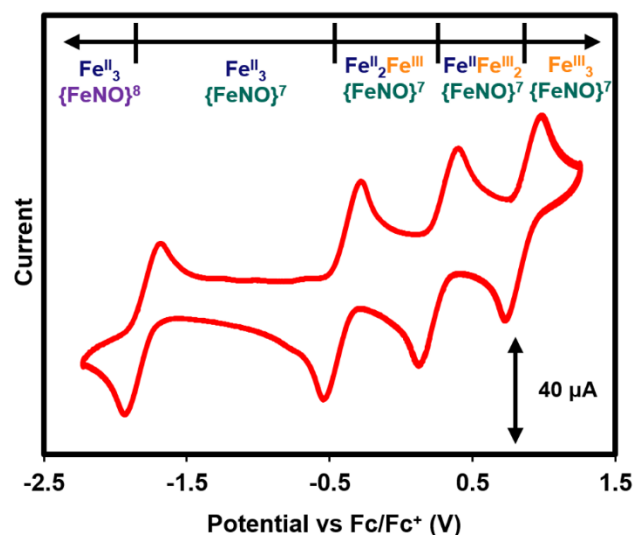


Figure 5. Cyclic voltammogram of monocationic nitrosyl cluster, **1-NO** (2mM) in CH_2Cl_2 with 100 mM $[\text{Bu}_4\text{N}][\text{PF}_6]$ at a scan rate of 200 mV/s with glassy carbon, Pt wire, and Ag wire as working, reference, and counter electrodes, respectively. The measured open-circuit potential was -0.7 V.

Mössbauer spectroscopy was performed on **1-NO** – **5-NO**. As observed in the $\mu_4\text{-O}$ system, Mössbauer parameters are consistent with oxidations being localized at the basal triiron core as characterized previously.^{8-9,14} In the Mössbauer spectrum of **1-NO**, the Fe–NO signal is readily distinguished from the basal iron centers in the cluster, and was fit with an isomer shift (δ) of 0.62 mm/s and a quadrupole splitting value ($|\Delta E_q|$) of 1.16 mm/s (Figure

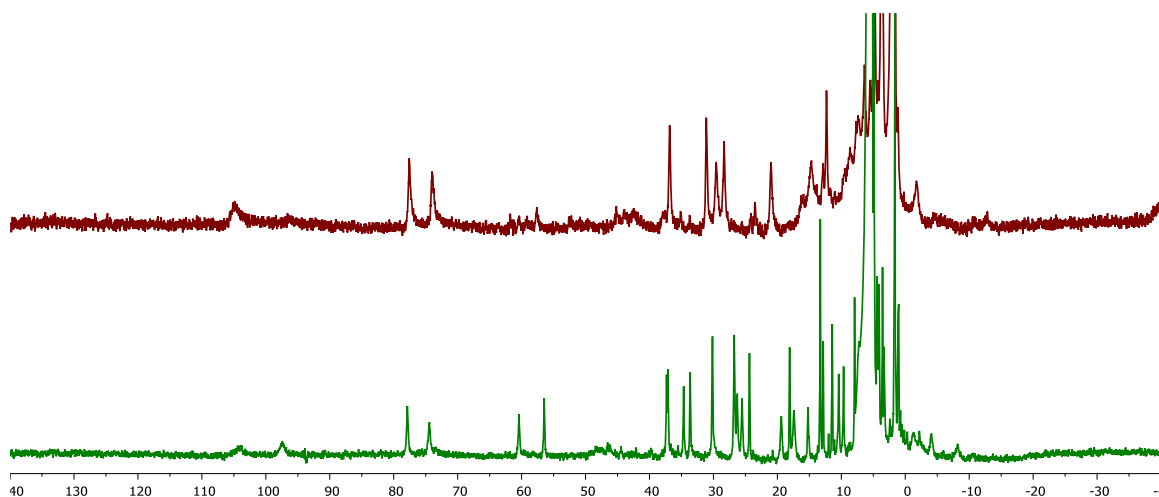


Figure 6. (Top) ^1H NMR (300 MHz; CD_3CN) of reaction mixture of **5-NO** in THF over 24 hours. The spectrum of the major species is identical to $[\text{LFe}_3\text{F}(\text{PhPz})_3\text{Fe}][\text{OTf}]$ (**1**) in CD_3CN . (Bottom) ^1H NMR (300 MHz; CD_2Cl_2) of reaction mixture of **5-NO** in THF over 24 hours. The spectrum of the new species is identical to $[\text{LFe}_3\text{O}(\text{PhPz})_3\text{Fe}][\text{OTf}]$. We have previously observed decomposition of $\text{LFe}_3\text{O}(\text{PhPz})_3\text{Fe}$ in dichloromethane to the monocationic cluster. This is consistent with formation of a mixture of $[\text{LFe}_3\text{F}(\text{PhPz})_3\text{Fe}]^+$ and $\text{LFe}_3\text{O}(\text{PhPz})_3\text{Fe}$ from the decomposition of **5-NO** in THF.

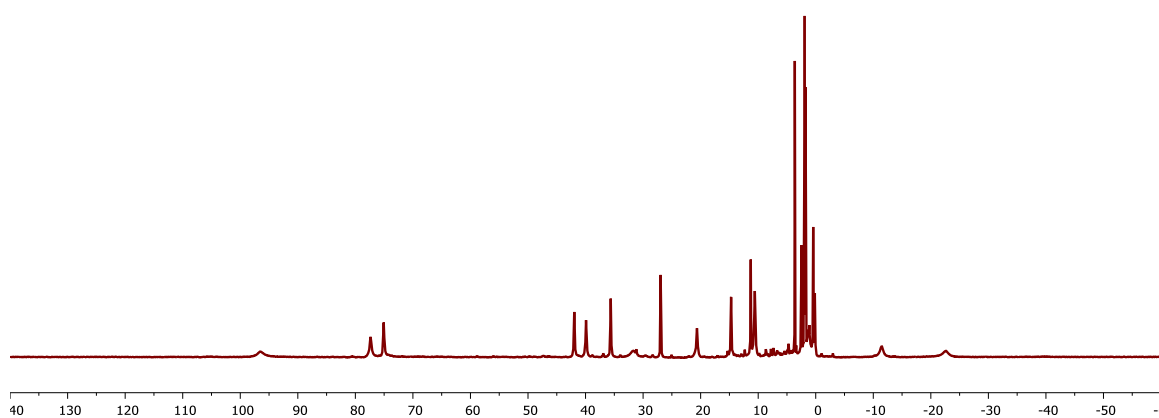


Figure 7. ^1H NMR (300 MHz; CD_3CN) of reaction mixture of AgOTf addition to $\text{LFe}_3\text{F}(\text{PhPz})_3\text{Fe}(\text{NO})$ (**5-NO**) in thawing THF. The spectrum is identical to $[\text{LFe}_3\text{F}(\text{PhPz})_3\text{Fe}(\text{NO})][\text{OTf}]$ (**1-NO**) in CD_3CN .

8B; Table 2). The exact Mössbauer parameters for the Fe–NO centers in **2-NO** – **4-NO** are more difficult to assign due to spectral overlap with signals from the Fe^{III} centers of the triiron core. The overlap is consistent, however, with only small changes in the Mössbauer parameters for the Fe–NO sites in **1-NO** – **4-NO** (Figures 8C-D and Table 2). These parameters are also similar to the previously reported μ_4 -O NO clusters, which have δ values ranging from 0.55 to 0.62 mm/s, and $|\Delta E_q|$ values of 1.94 to 2.38 mm/s.⁸ Overall, these data, along with the IR spectroscopy data (vide infra), are consistent with the {FeNO}⁷ formulation, according to

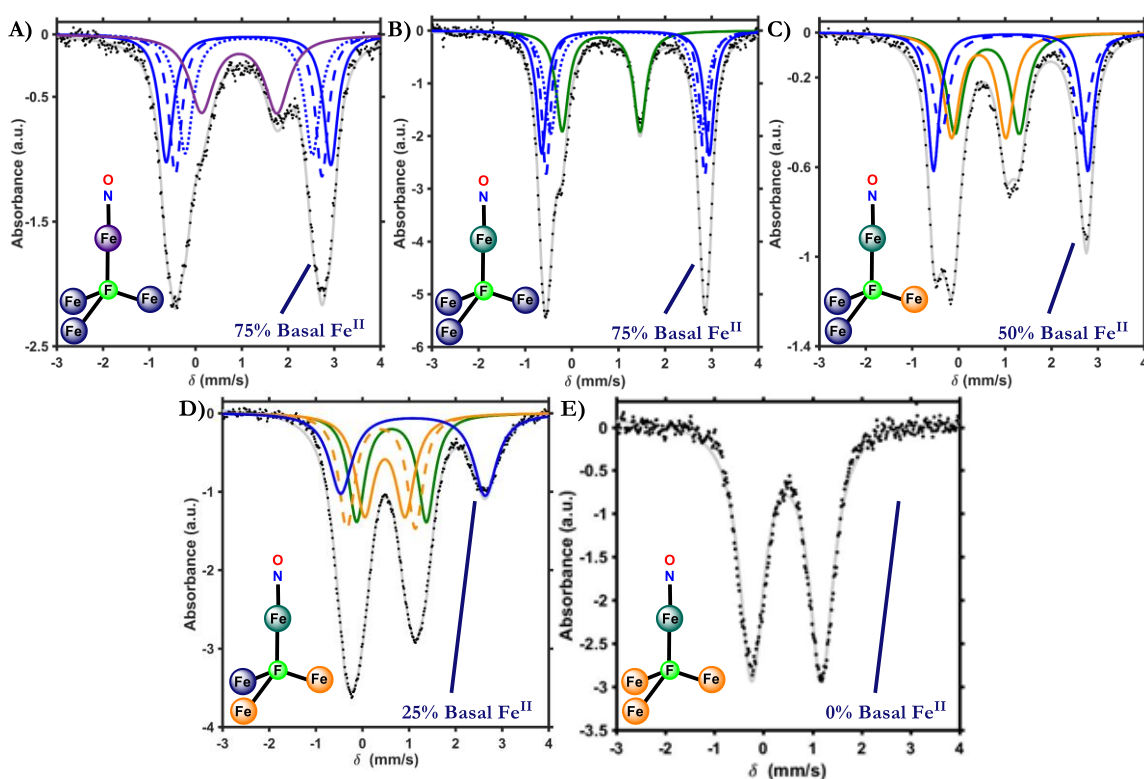


Figure 8. Zero applied field ⁵⁷Fe Mössbauer spectra at 80K of (A) **5-NO**, (B) **1-NO**, (C) **2-NO**, (D) **3-NO**, and (E) **4-NO**. Black dots represent the data, gray traces are the sum of the simulated fits, and colored traces represent the individual fits for the Fe centers (see Table 2 for parameters). Blue traces represent assignments made to basal Fe^{II}, orange traces represent basal Fe^{III} assignments, green and purple traces represent {FeNO}⁷ and {FeNO}⁸ units, respectively.

Table 2. Fe- μ_4 -F Distances and ^{57}Fe Mössbauer Parameters for Complexes 1-NO – 5-NO with Oxidation State Assignments

Fe Center	Fe- μ_4 -F distance (Å)	δ (mm/s)	$ \Delta E_q $ (mm/s)	assignment
1-NO				
Fe1, Fe2, Fe3	2.129(7); 2.205(6); 2.169(5)	1.15; 1.15; 1.16	3.59; 3.40; 3.23	h.s. Fe ^{II}
Fe4	2.065(7)	0.63	1.67	{FeNO} ⁷
2-NO				
Fe1	2.030(4)	0.44	1.17	<i>h.s.</i> Fe ^{III}
Fe2, Fe3	2.237(4); 2.101(4)	1.12; 1.15	3.31; 3.03	<i>h.s.</i> Fe ^{II}
Fe4	2.093(4)	0.62	1.39	{FeNO} ⁷
3-NO				
Fe1	2.207(3)	1.09	3.10	<i>h.s.</i> Fe ^{II}
Fe2, Fe3	2.080(3); 2.091(3)	0.48; 0.40	0.87; 1.47	<i>h.s.</i> Fe ^{III}
Fe4	2.155(3)	0.62	1.51	{FeNO} ⁷
4-NO^a				
Fe1-Fe4	-	0.47	1.42	<i>h.s.</i> Fe ^{III} and {FeNO} ⁷
5-NO				
Fe1, Fe2, Fe3	-	1.15; 1.15; 1.15	3.56; 3.17; 3.75	h.s. Fe ^{II}
Fe4	-	0.95	1.63	{FeNO} ⁸

^aIn this case, the signals for the Fe centers overlap preventing reliable parameter determination for the unique apical {FeNO}⁷ center. The presence of an {FeNO}⁷ moiety is supported via the IR spectroscopy data.

Enemark-Feltham notation.¹⁵ The Mössbauer spectrum of **5-NO** was fit with three Fe^{II} in the triiron core and an apical Fe-NO signal distinct from the ones observed for **1-NO** – **4-NO**; this is assigned as {FeNO}⁸ ($\delta = 0.94$ mm/s and $|\Delta E_q| = 1.63$ mm/s; Figure 8A), consistent with reduction of the Fe-NO moiety rather than a remote metal site. Compounds **1-NO**, **2-NO**, and **3-NO** were structurally characterized by XRD. In all cases, binding of NO to the apical Fe occurs in a linear fashion ($\angle \text{Fe4-N40-O40} > 175^\circ$, Figure 9A). As observed in the μ_4 -O system and from Mössbauer spectra (Figure 8B-D), bond metrics are consistent

with oxidations being localized at the basal triiron core of these three clusters (Table 2). The Fe- μ_4 -F bonds, which range from 2.07 to 2.24 Å, are longer than the Fe- μ_4 -O bonds (1.93 to 2.18 Å) despite the shorter ionic radius of F⁻ which suggests a significantly weaker interaction with the fluoride resulting in more electron deficient metal centers.¹⁶

IR spectroscopy reveals a large range of $\nu_{\text{N-O}}$ for complexes **1-NO** – **5-NO**, from 1680 cm⁻¹ to 1855 cm⁻¹ (Figure 10). Comparison of $\nu_{\text{N-O}}$ for **1-NO** – **4-NO** (1799 – 1855 cm⁻¹) provides insight into the effect of remote redox changes on NO activation. Oxidation of the Fe centers not bound to NO leads to an average of 19 cm⁻¹ per redox change, with redox changes of more reduced clusters having a larger effect. The shift in $\nu_{\text{N-O}}$ to higher energy upon oxidation is matched by an increase in Fe4- μ_4 -F distance, and likely results from a more electron deficient Fe4 center due to this elongation. The nature and type of interaction with axial ligand has been previously demonstrated to effect the level of NO activation in mononuclear Fe complexes.¹⁷ Analogous shifts in the distance between Fe and axial ligands trans to coordinated N₂ have been reported for monoiron models of nitrogenase.¹⁸

The correlation between the increase in the Fe4- μ_4 -ligand distance and the increase in the $\nu_{\text{N-O}}$ frequency observed previously for μ_4 -O and now with μ_4 -F interstitial ligands suggests that this structural parameter generally serves to relay the effect of remote redox changes to the metal that binds the small molecule. However, the magnitude of the change in NO activation as a result of these distal redox changes varies with the nature of the interstitial atom. For μ_4 -O clusters, the $\nu_{\text{N-O}}$ changes from 1715/1759 to 1823 cm⁻¹ over two redox events with an average change of 54/33 cm⁻¹ per electron transfer, in contrast to only 19 cm⁻¹ for μ_4 -F. The stronger O²⁻ ligand roughly doubles the effect of the remote redox changes on the activation of NO compared to F⁻. This is a unique observation, which relies on the ability to access multiple oxidation states of these clusters, and demonstrates that an interstitial ligand

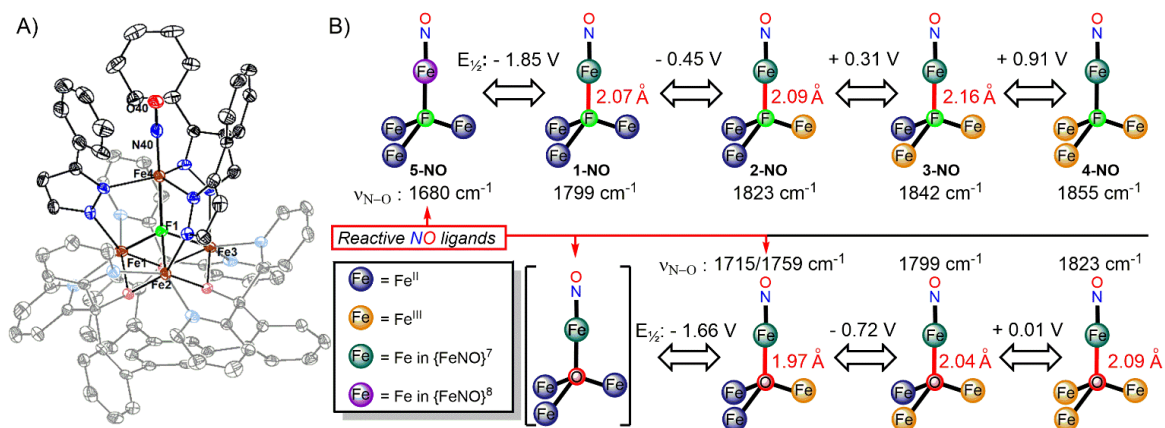


Figure 9. (A) Crystal structure of tetranuclear iron nitrosyl cluster **2-NO** with ellipsoids shown at the 50% probability level. Solvents molecules, outer-sphere counterions, and H atoms are omitted for clarity. (B) Simplified depiction of the tetranuclear iron clusters discussed. Measured redox potentials, NO stretching frequencies, and apical Fe- μ_4 -ligand distances are included for comparison. Data for the μ_4 -O clusters were previously reported.⁸

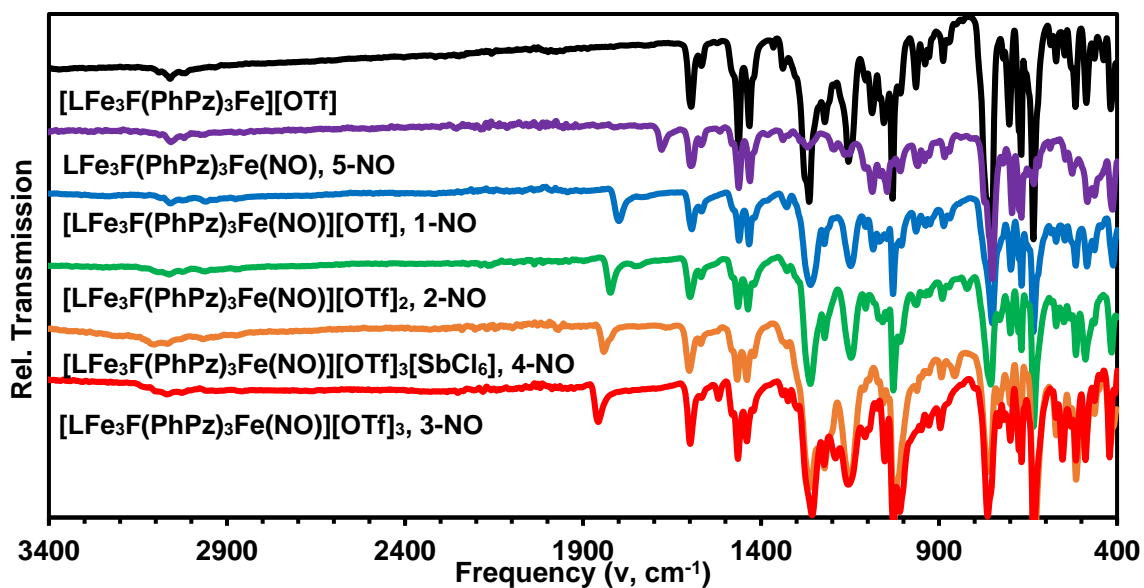


Figure 10. Solid state IR spectra of complexes **1**, **1-NO** - **5-NO**.

can influence small molecule activation in two ways: first, by its direct interaction with the small molecule-binding metal center, and second, by modulation of the degree to which other

metals in the cluster can perturb this meta-interstitial ligand interaction. A structural comparison of the Fe4- μ_4 -ligand distances over two oxidation states shows that redox changes at the remote Fe centers shift the Fe4- μ_4 -F distance by 0.09 Å and the Fe4- μ_4 -O bond by 0.12 Å (Figure 9B). The more donating interstitial ligand is able to more efficiently translate remote redox changes in the cluster into NO activation.

A consequence of varying the μ_4 -ligand in these clusters is that the weaker F⁻ donor increases the overall cluster charge of a particular redox state by 1 compared to the O²⁻ version. In reported mononuclear complexes, related modifications of a ligand's charge at a distal site (i.e. R₃BH⁻ vs R₃CH) leads to observable shifts of bound carbonyl stretching frequencies by ~10 – 40 cm⁻¹.¹⁹ For these clusters, separating the effect of higher positive charge from the effect of the donating abilities of the interstitial ligand on NO activation can be addressed by comparing clusters **2-NO-4-NO** and the μ_4 -O analogues. For the same cluster redox state, significantly higher $\nu_{\text{N-O}}$ are observed for the μ_4 -F ligand compared to μ_4 -O, as expected. The overall cluster charge, which is higher by 1 compared to μ_4 -O clusters of the same Fe redox states, is not sufficient to explain the higher NO activation. A comparison of clusters of the same charge for μ_4 -O and μ_4 -F, but higher overall Fe redox state for μ_4 -O (for example, (μ_4 -F)Fe^{II}Fe^{III}₂{FeNO}⁷ (**3-NO**) with $\nu_{\text{N-O}}$ = 1842 cm⁻¹ vs (μ_4 -O)Fe^{III}₂{FeNO}⁷ with $\nu_{\text{N-O}}$ = 1823 cm⁻¹) still shows a higher degree of NO activation with O²⁻. This difference suggests that the higher-charge interstitial ligand leads to a more electron-rich cluster and a lower $\nu_{\text{N-O}}$ due to its direct interaction with the metal centers rather than *solely* due to the reduced cluster charge.

IR spectroscopy of **5-NO** corroborates the Mössbauer data and is consistent with the formation of a {FeNO}⁸ motif; the $\nu_{\text{N-O}}$ at 1680 cm⁻¹, is ~120 cm⁻¹ lower than $\nu_{\text{N-O}}$ for the {FeNO}⁷ moiety of **1-NO**. A similarly large shift was observed upon reduction for a structurally related mononuclear trigonal bipyramidal Fe-NO complex,²⁰ and more generally

for nonheme $\{\text{FeNO}\}^7/\{\text{FeNO}\}^8$ complexes.²¹ An analogous species is not observable for the $\mu_4\text{-O}$ clusters. A comparison of the redox potentials of the $\mu_4\text{-F}$ and the $\mu_4\text{-O}$ systems (Figure 9B)⁸ reveals that the F^- ligand shifts the redox potentials positively by approximately 1 V for the same cluster oxidation states compared to the O^{2-} ligand because of the lower negative charge and weaker electron donating ability of F^- . An analogous effect is observed for other clusters upon changing the bridging ligand to alter the charge of the cluster.^{6, 7e} The shift in redox potentials allows access to more reduced states of the $\mu_4\text{-F}$ clusters within the electrochemical solvent window, which could be beneficial for storing additional reducing equivalents at more positive potentials. However, this is counterbalanced by weaker activation of the diatomic ligand, as reflected by IR spectroscopy (vide supra). In fact, to achieve the same level of NO activation, the $\mu_4\text{-F}$ clusters need to have Fe oxidation states lower by two levels compared to the $\mu_4\text{-O}$ clusters. This is in contrast to the behavior observed for certain iron-multicarbonyl clusters, where data is available for isostructural motifs. For example, $[\text{Fe}_4\text{C}(\text{CO})_{12}]^{2-}$ shows lower average CO activation than the one electron more reduced, but same-charge cluster, $[\text{Fe}_4\text{N}(\text{CO})_{12}]^{2-}$.^{6, 22} The difference is likely a result of distribution of charge and small molecule activation over many (12) CO ligands. In the present system, which displays a more biomimetic, single ligand binding, the NO activation is relayed remotely through the interstitial atom and provides a test for the ability of the μ_4 ligand to communicate the redox change at metals not bound to NO. Furthermore, differences in chemical reactivity of the diatomic ligand are observed. The addition of NO to $(\mu_4\text{-O})\text{Fe}^{\text{II}}_2\text{Fe}^{\text{III}}\{\text{FeNO}\}^7$ leads to NO disproportionation to generate N_2O and the one electron oxidized nitrosyl cluster.⁸ In contrast, addition of NO to **1-NO**, which is one electron more reduced $(\mu_4\text{-F})\text{Fe}^{\text{II}}_3\{\text{FeNO}\}^7$, does not result in a reaction. This difference in reactivity as a function of interstitial ligand is likely due to a more activated NO and a 250 mV lower redox potential for the $\mu_4\text{-O}$ cluster.

Only **5-NO**, with an electronically different, $\{\text{FeNO}\}^8$ moiety, undergoes conversion to N_2O with a fluoride interstitial ligand, albeit not cleanly. Overall, despite more negative potentials compared to $\mu_4\text{-F}$ analogs of the same redox state, reactivity of NO is observed at milder potentials with the $\mu_4\text{-O}$ cluster.

CONCLUSIONS

In this report, we have demonstrated the significant effects that the change of interstitial ligands ($\mu_4\text{-O}$ vs $\mu_4\text{-F}$) has on the small molecule activation properties of tetranuclear Fe clusters. The more positive redox potentials of $\mu_4\text{-F}$ clusters allow access to more reduced Fe states. However, this does not result in more efficient activation of small molecule ligands, as inferred from IR spectroscopy and reactivity of NO complexes. The higher $\nu_{\text{N-O}}$ values of the $\mu_4\text{-F}$ species for the same Fe oxidation states compared to the $\mu_4\text{-O}$ analogues are not due to the difference in cluster charge but rather the nature of the interactions with the bridging ligand. To achieve similar NO activation, the cluster needs to be two electrons more reduced with the $\mu_4\text{-F}$ compared to the $\mu_4\text{-O}$ ligand. Consequently, NO disproportionation is observed with a $\mu_4\text{-O}$ ligand at higher Fe oxidation states and more positive potentials than with a $\mu_4\text{-F}$ ligand. Furthermore, the $\mu_4\text{-O}$ ligand is a better relay of remote redox changes. The structure-function studies described here suggest that a higher charge interstitial ligand, such as the carbide in FeMoco of nitrogenase, is more efficient at tuning cluster properties in a variety of ways toward the activation of small molecule. Cluster analogs with interstitial C and N moieties are currently being pursued for comparison.

EXPERIMENTAL DETAILS

General Considerations. All reactions were performed at room temperature in an N₂-filled M. Braun glovebox or using standard Schlenk techniques unless otherwise specified. Glassware was oven dried at 140 °C for at least 2 h prior to use, and allowed to cool under vacuum. **LFe₃(OAc)(OTf)₂**,⁸ Fe(N(SiMe₃)₂)₂,²³ benzyl potassium,²⁴ 1-*H*-3-phenyl pyrazole (HPhPz),²⁵ anhydrous [NBu₄][F]²⁶, and [(2,4-Br-C₆H₃)₃N][SbCl₆]²⁷ were prepared according to literature procedures. [(4-Br-C₆H₄)₃N][OTf] was prepared according to a modified literature procedure.²⁸ Tetrahydrofuran was dried using sodium/benzophenone ketyl, degassed with three freeze-pump-thaw cycles, vacuum transferred, and stored over 3Å molecular sieves prior to use. CH₂Cl₂, diethyl ether, benzene, acetonitrile, hexanes, and pentane were dried by sparging with nitrogen for at least 15 minutes, then passing through a column of activated A2 alumina under positive N₂ pressure. ¹H and ¹⁹F NMR spectra were recorded on a Varian 300 MHz spectrometer. ¹³C NMR spectra were recorded on a Varian 500 MHz spectrometer. CD₃CN and CD₂Cl₂ was purchased from Cambridge Isotope Laboratories, dried over calcium hydride, degassed by three freeze-pump-thaw cycles, and vacuum transferred prior to use. Infrared (ATR-IR) spectra were recorded on a Bruker ALPHA ATR-IR spectrometer at 4 cm⁻¹ resolution. Headspace analysis was conducted on a HP 5972 GC-MS.

Physical Methods. Mössbauer measurements. Zero applied field ⁵⁷Fe Mossbauer spectra were recorded at 80 K in constant acceleration mode on a spectrometer from See Co (Edina, MN) equipped with an SVT-400 cryostat (Janis, Wilmington, WA). The isomer shifts are relative to the centroid of an α-Fe foil signal at room temperature. Samples were prepared by mixing polycrystalline material (20 mg) with boron nitride in a cup fitted with screw cap or freezing a concentrated acetonitrile solution in the cup. The data were fit to Lorentzian lineshapes using WMOSS (www.wmoss.org).

Mössbauer simulation details for compounds 1 – 3 and 1-NO – 5-NO. All spectra were simulated as four pairs of symmetric quadrupole doubles with equal populations and Lorentzian lineshapes (the parameter defining the width, Γ , is reported). They were refined to a minimum via least squares optimization (13 fitting parameters per spectrum). Signals appearing above 2 mm/s were indicative with the presence of high-spin Fe^{II} centers and correspond to species with isomer shifts ~ 1 mm/s. The Mössbauer data were fit to be consistent with our previously reported iron clusters.^{8-9,14} The observed Mossbauer parameters are in agreement with related six-coordinate high-spin Fe^{II}/Fe^{III} centers.²⁹

Electrochemical measurements. CVs and SWVs were recorded with a Pine Instrument Company AFCBP1 biopotentiostat with the AfterMath software package. All measurements were performed in a three electrode cell, which consisted of glassy carbon (working; $\phi = 3.0$ mm), silver wire (counter), and bare platinum wire (reference), in a N₂ filled M. Braun glovebox at RT. Dry acetonitrile or CH₂Cl₂ that contained ~ 85 mM [Bu₄N][PF₆] was used as the electrolyte solution. The ferrocene/ferrocinium (Fc/Fc⁺) redox wave was used as an internal standard for all measurements.

X-ray crystallography. X-ray diffraction data was collected at 100 K on a Bruker PHOTON100 CMOS based diffractometer (microfocus sealed X-ray tube, Mo K α (λ) = 0.71073 Å or Cu K α (λ) = 1.54178 Å). All manipulations, including data collection, integration, and scaling, were carried out using the Bruker APEXII software. Absorption corrections were applied using SADABS. Structures were solved by direct methods using XS (incorporated into SHELXTL) and refined by using ShelXL least squares on Olex2-1.2.7 to convergence. All non-hydrogen atoms were refined using anisotropic displacement parameters. Hydrogen atoms were placed in idealized positions and refined using a riding model. Due to the size of

the compounds (**1 - 3** and **1-NO – 3-NO**), most crystals included solvent-accessible voids that contained disordered solvent. In most cases the solvent could be modeled satisfactorily.

Synthetic Procedures. *Synthesis of Potassium 3-phenyl-pyrazolate (KPhPz).* In the glovebox, a solution of 1-*H*-3-phenyl-pyrazole (1.54 g, 11.8 mmol) in THF (5 mL) was stirred while a solution of benzyl potassium (1.70 g, 11.8 mmol) in THF (10 mL) was added drop-wise. Addition caused the solution to change from colorless to pale yellow. After 30 minutes, the solvent was removed under reduced pressure to obtain 1.83 g off-white powder (85% yield). ¹H NMR (300 MHz, CD₃CN) δ 7.83 (d, 2H), 7.44 (s, 1H), 7.28 (t, 2H), 7.07 (t, 1H), 6.39 (s, 1H). ¹³C NMR (500 MHz, CD₃CN) δ 100.01 (Pz NCCH), 125.02 (*p*-Ar CH), 125.37 (*m*-Ar CH), 128.98 (*o*-Ar CH), 139.34 (Pz CHCHN), 150.27 (Pz NCCH). An expected signal ~ 138 ppm (*i*-Ar C)⁸ could not be observed, likely due to the low solubility of KPhPz.

Synthesis of tris-4-bromo-phenylamininum trifluoromethanesulfonate ([*(4-Br-C₆H₄)₃N*][OTf]). This was prepared through a modification of a literature procedure for [*(4-Br-C₆H₄)₃N*][BF₄].²⁸ Tris-4-bromo-phenylamine (1.5 g, 3.11 mmol) was dissolved in 30 mL diethyl ether with silver trifluoromethanesulfonate (AgOTf; 1.2 g, 4.67 mmol). This light green solution was added to a 100 mL Schlenk tube and cooled to -40 °C under N₂ atmosphere. Iodine powder (0.75 g, 2.96 mmol) was added with a counter-flow of N₂ while stirring; addition caused the solution to turn dark blue. The Schlenk tube was warmed to room temperature and filtered over a coarse porosity frit. The collected precipitate was filtered with 30 mL CH₂Cl₂ in the glovebox. To the resulting dark blue solution, 40 mL diethyl ether was added and the flask was cooled to -40 °C. [*(4-Br-C₆H₄)₃N*][OTf] was collected as a dark purple solid upon filtration (1.36 g, 69% yield). Anal. Calc. (%) for C₁₉H₁₂Br₃F₃NO₃S: C, 36.16; H, 1.92; N, 2.22. Found: C, 36.70; H, 1.94; N, 2.27.

Synthesis of [LFe₃F(PhPz)₃Fe][OTf] (1). In the glovebox, a suspension of **LFe₃(OAc)(OTf)₂** (1047 mg, 0.76 mmol) in THF (3 mL) was frozen in the cold well. To the thawing suspension, solutions of potassium 3-phenyl-pyrazolate (190 mg, 1.04 mmol) in THF (3 mL) and 1-*H*-3-phenyl-pyrazole (220 mg, 1.52 mmol) in THF (3 mL) were added. The suspension changed color from yellow to orange upon addition of the potassium 3-phenyl-pyrazolate. [Bu₄N][F] (208 mg, 0.79 mmol) was added as a suspension in THF (3 mL), causing the solution to become dark red. A solution of Fe(N(SiMe₃)₂)₂ (288 mg, 0.76 mmol) in THF (2 mL) was added. The reaction was stirred for 20 h, after which an orange precipitate was observed. The suspension was filtered over a bed of celite on a fine porosity glass frit and washed with 5 mL THF. The orange solid was collected with 60 mL MeCN. The solvent was removed under reduced pressure to obtain [LFe₃F(PhPz)₃Fe][OTf] as an orange solid (950 mg, 75% yield). ¹H NMR (300 MHz, CD₂Cl₂) δ 104.77, 78.57, 75.13, 48.82, 37.46, 30.48, 27.17, 26.44, 25.63, 19.69, 18.42, 11.60, 10.53, 4.54, 4.22, 3.44, 1.99, 1.27, 1.16, -1.13, -2.80, -46.96. ¹⁹F NMR (300 MHz, CD₂Cl₂) δ -78.45. UV-vis (CH₂Cl₂) [ε (M⁻¹ cm⁻¹): 251 nm (9.2 × 10⁴), 463 nm (3.9 × 10³). Anal. Calcd. (%) for C₈₅H₆₀F₄Fe₄N₁₂O₆S: C, 60.88; H, 3.61; N, 10.02. Found: C, 61.16; H, 3.75; N, 9.74.

Synthesis of [LFe₃F(PhPz)₃Fe][OTf]₂ (2). To a suspension of [LFe₃F(PhPz)₃Fe][OTf] (**1**; 94 mg, 0.06 mmol) in THF (2 mL), a solution of AgOTf (14 mg, 0.06 mmol) in THF (2 mL) was added. The color of the suspension changed from orange to brown and, after 2 hours, the solvent was removed under reduced pressure. The brown residue was dissolved in CH₂Cl₂ and filtered over a bed of celite on glass filter paper. The solvent was removed under reduced pressure to obtain [LFe₃F(PhPz)₃Fe][OTf]₂ as a brown solid (100 mg, 98% yield). ¹H NMR (300 MHz, CD₂Cl₂) δ 101.33, 87.83, 79.33, 47.73, 46.79, 35.24, 34.14, 28.86, 26.35, 18.15, 16.58, 16.33, 12.10, 8.55, 7.28, 6.79, 6.25, 5.25, 4.63, -42.36. ¹⁹F NMR (300 MHz, CD₂Cl₂) -

78.19. UV-vis (CH_2Cl_2) [ϵ ($\text{M}^{-1} \text{cm}^{-1}$): 250 nm (10.9×10^4), 432 nm (4.8×10^3). Anal. Calcd. (%) for $\text{C}_{86}\text{H}_{60}\text{F}_7\text{Fe}_4\text{N}_{12}\text{O}_9\text{S}_2$: C, 56.57; H, 3.31; N, 9.21. Found: C, 56.47; H, 3.13; N, 8.88.

*Synthesis of $[\text{LFe}_3\text{F}(\text{PhPz})_3\text{Fe}(\text{MeCN})][\text{OTf}]_3$ (**3**).* To a stirring solution of $[\text{LFe}_3\text{F}(\text{PhPz})_3\text{Fe}][\text{OTf}]_2$ (**2**; 78.5 mg, 0.04 mmol) in acetonitrile (2 mL), $[(\text{p-Br-C}_6\text{H}_4)_3\text{N}][\text{OTf}]$ (27.1 mg, 0.04 mmol) was added as an MeCN solution (2 mL). The brown solution became purple upon addition. After 30 minutes, the solution was filtered. 5 mL of CH_2Cl_2 was added to the filtrate, then 10 mL pentane, to obtain a purple precipitate. The supernatant was decanted and the remaining solid was briefly dried under reduced pressure to obtain $[\text{LFe}_3\text{F}(\text{PhPz})_3\text{Fe}(\text{MeCN})][\text{OTf}]_3$ as a purple solid (42.3 mg, 50% yield). ^1H NMR (300 MHz, CD_3CN) δ 125.15, 91.53, 82.45, 80.10, 61.48, 51.98, 43.99, 15.30, 13.93, 12.33, 8.44, 6.48, 5.67, 5.30, 0.46, -5.74, -18.78. ^{19}F NMR (300 MHz, CD_3CN) -75.66. UV-vis (CH_2Cl_2) [ϵ ($\text{M}^{-1} \text{cm}^{-1}$): 250 nm (10.3×10^4), 465 nm (3.6×10^3). Anal. Calcd. (%) for $\text{C}_{88}\text{H}_{62}\text{Cl}_2\text{F}_{10}\text{Fe}_4\text{N}_{12}\text{O}_{12}\text{S}_3$ (**3** with CH_2Cl_2 instead of MeCN; compound recrystallized in CH_2Cl_2): C, 51.31; H, 3.03; N, 8.16. Found: C, 51.26; H, 3.04; N, 8.43.

*Synthesis of $[\text{LFe}_3\text{F}(\text{PhPz})_3\text{Fe}(\text{NO})][\text{OTf}]$ (**1-NO**).* *Method A.* In the glovebox, a 100 mL Schlenk tube was charged with a solution of $[\text{LFe}_3\text{F}(\text{PhPz})_3\text{Fe}][\text{OTf}]$ (**1**; 179 mg, 0.11 mmol) in CH_2Cl_2 (5 mL). The solution was degassed by three freeze-pump-thaw cycles. While frozen, gaseous nitric oxide (33 mL, 59 mmHg, 0.11 mmol) was condensed in the tube. The reaction was stirred at room temperature for 2 h and changed color from orange to brown. The solvent was removed under reduced pressure to yield $[\text{LFe}_3\text{F}(\text{PhPz})_3\text{Fe}(\text{NO})][\text{OTf}]$ as a brown solid (181 mg, 99% yield). ^1H NMR (300 MHz, CD_2Cl_2) δ 98.43, 76.64, 74.24, 42.59, 40.12, 35.92, 32.51, 27.06, 20.05, 15.27, 14.16, 11.24, 10.79, 4.27, 2.46, 1.13, 0.58, 0.46, -10.77, -23.61. ^{19}F NMR (300 MHz, CD_2Cl_2) δ -78.71. Anal. Calcd. (%) for $\text{C}_{86}\text{H}_{62}\text{Cl}_2\text{F}_4\text{Fe}_4\text{N}_{13}\text{O}_7\text{S}$ (**1-NO** ·

CH₂Cl₂; compound recrystallized from CH₂Cl₂/pentane): C, 57.66; H, 3.49; N, 10.16. Found: C, 57.40; H, 3.46; N, 10.01.

Method B. In the glovebox, solid LFe₃F(PhPz)₃Fe(NO) (**5-NO**; 22 mg, 0.014 mmol) was cooled to -196 °C in a cold well in a 20 mL vial with a stir bar. AgOTf (3.7 mg, 0.014 mmol) in 0.5 mL thawing tetrahydrofuran was added to the cooled powder. This reaction was stirred at room temperature for 30 minutes then pumped down. The purple suspension became a brown solution. ¹H NMR analysis of the crude reaction showed mostly (>90%) [LFe₃F(PhPz)₃Fe(NO)][OTf] (**1-NO**). The brown solid was filtered in CH₂Cl₂ to obtain 16.8 mg of [LFe₃F(PhPz)₃Fe(NO)][OTf] after recrystallization (69% yield).

*Synthesis of [LFe₃F(PhPz)₃Fe(NO)][OTf]₂ (**2-NO**).* *Method A.* In the glovebox, a 100 mL Schlenk tube was charged with a solution of [LFe₃F(PhPz)₃Fe][OTf]₂ (**2**; 163 mg, 0.09 mmol) in CH₂Cl₂ (5 mL). The solution was degassed by three freeze-pump-thaw cycles. While frozen, gaseous nitric oxide (33 mL, 50 mmHg, 0.09 mmol) was condensed in the tube. The reaction was stirred at room temperature for 2 h, changing color from brown to yellow-green. The solvent was removed under reduced pressure to yield [LFe₃F(PhPz)₃Fe(NO)][OTf]₂ as a dark green solid (162 mg, 98% yield). ¹H NMR (300 MHz, CD₂Cl₂) δ 100.10, 83.22, 80.63, 66.68, 50.74, 46.79, 41.32, 17.25, 14.62, 14.38, 12.35, 11.71, 3.31, 0.30, -3.31, -17.33. ¹⁹F (300 MHz, CD₂Cl₂) δ -77.52. Anal. Calcd. (%) for C₈₆H₆₀F₇Fe₄N₁₃O₁₀S₂: C, 55.65; H, 3.26; N, 9.81. Found: C, 55.59; H, 3.25; N, 9.53.

Method B. In the glovebox, a solution of [LFe₃F(PhPz)₃Fe(NO)][OTf] (**1-NO**; 160 mg, 0.10 mmol) in MeCN (3 mL) was added to a solution of AgOTf (25 mg, 0.10 mmol) in MeCN (2 mL). The solution changed color from brown to yellow-green. After 1 h, the solvent was removed under reduced pressure. The green residue was dissolved in CH₂Cl₂ and filtered over a bed of celite. The solvent was removed under reduced pressure to obtain

$[\text{LFe}_3\text{F}(\text{PhPz})_3\text{Fe}(\text{NO})][\text{OTf}]_2$ as a dark green solid (164 mg, 95% yield). ^1H NMR is identical to that observed for method A.

*Synthesis of $[\text{LFe}_3\text{F}(\text{PhPz})_3\text{Fe}(\text{NO})][\text{OTf}]_3$ (**3-NO**).* In the glovebox, a solution of $[\text{LFe}_3\text{F}(\text{PhPz})_3\text{Fe}(\text{NO})][\text{OTf}]_2$ (**2-NO**; 27.6 mg, 0.015 mmol) in CH_2Cl_2 (1 mL) was stirred as a solution of $[(4\text{-Br-C}_6\text{H}_4)_3\text{N}][\text{OTf}]$ (10.0 mg, 0.016 mmol) in CH_2Cl_2 (1 mL) was added. The addition caused the yellow-green solution to turn purple. After 30 minutes, the reaction was filtered and layered under pentane to afford purple crystals of $[\text{LFe}_3\text{F}(\text{PhPz})_3\text{Fe}(\text{NO})][\text{OTf}]_3$ (20.3 mg, 68% yield). ^1H NMR (300 MHz, CD_2Cl_2) δ 123.58, 98.80, 89.32, 60.89, 41.42, 14.25, 13.41, 10.34, 5.32, 4.35, 3.93, 3.71, 3.47, 2.07, 1.85, 1.18, -2.45, -8.26. Anal. Calcd. (%) for $\text{C}_{87}\text{H}_{60}\text{F}_{10}\text{Fe}_4\text{N}_{13}\text{O}_{13}\text{S}_3$: C, 52.12; H, 3.02; N, 9.08. Found: C, 51.88; H, 2.94; N, 8.74.

*Synthesis of $[\text{LFe}_3\text{F}(\text{PhPz})_3\text{Fe}(\text{NO})][\text{OTf}]_3[\text{SbCl}_6]$ (**4-NO**).* In the glovebox, a thawing solution of $[\text{LFe}_3\text{F}(\text{PhPz})_3\text{Fe}(\text{NO})][\text{OTf}]_3$ (**3-NO**; 25.7 mg, 0.013 mmol) in CH_2Cl_2 (1 mL) was stirred as a solution of $[(2,4\text{-Br-C}_6\text{H}_3)_3\text{N}][\text{SbCl}_6]$ (13.9 mg, 0.013 mmol) in MeCN (1 mL) was added. The addition caused the purple solution to turn blue. Cold toluene was added until a precipitate was observed. This was kept in a liquid nitrogen-cooled cold well for 2 minutes. The supernatant was decanted and the resulting solid was dried under vacuum. This afforded $[\text{LFe}_3\text{F}(\text{PhPz})_3\text{Fe}(\text{NO})][\text{OTf}]_3[\text{SbCl}_6]$ as a blue solid (15 mg, 49% yield). This compound decomposes over time in solution and the solid state, even at reduced temperatures. Characterization of this compound was conducted with freshly prepared samples to minimize decomposition. ^1H NMR (300 MHz, CD_3CN) δ 124.54, 97.65, 80.33, 77.50, 74.55, 37.57, 18.30, 15.25, 13.39, 9.04, 0.01, -1.66, -5.71, -6.88. Anal. Calcd. (%) for $\text{C}_{101}\text{H}_{76}\text{Cl}_6\text{F}_{10}\text{Fe}_4\text{N}_{13}\text{O}_{13}\text{S}_3\text{Sb}$ ($^{\text{NO}}\mathbf{4} \cdot 2 \text{C}_7\text{H}_8$; compound precipitated with toluene): C, 48.07; H, 3.04; N, 7.21. Found: C, 47.83; H, 2.97; N, 7.88.

*Synthesis of $LFe_3F(PhPz)_3Fe(NO)$ (**5-NO**).* In the glovebox, a solution of $[LFe_3F(PhPz)_3Fe(NO)][OTf]$ (**1-NO**; 82.9 mg, 0.049 mmol) in MeCN was stirred as a solution of $CoCp^*_2$ (16.8 mg, 0.051 mmol) in MeCN was added. The addition caused the brown solution to become a purple suspension. After 2 hours, the solids were collected, washed with minimal MeCN, and dried under vacuum to afford $LFe_3F(PhPz)_3Fe(NO)$ as a purple solid (44.3 mg, 59% yield). This species decomposes upon dissolution in tetrahydrofuran, pyridine, or CH_2Cl_2 and is mostly insoluble in acetonitrile, benzene, and toluene. Therefore, NMR and UV-Vis Absorbance data could not be collected for this complex. Anal. Calcd. (%) for $C_{84}H_{60}FFe_4N_{13}O_4$: C, 64.76; H, 3.88; N, 11.69. Found: C, 64.21; H, 3.86; N, 11.51.

*Decomposition of $LFe_3F(PhPz)_3Fe(NO)$ (**5-NO**).* In the glovebox, solid $LFe_3F(PhPz)_3Fe(NO)$ (26 mg, 0.02 mmol) was added to a 20 mL vial with septum cap and stir bar. 10 mL tetrahydrofuran was added and the vial was quickly sealed. Upon dissolving, the solution appeared brown. After stirring for 24 hr, the headspace was analyzed via GC-MS. A blue precipitate was observed in a brown-orange solution.

ELECTROCHEMICAL DETAILS

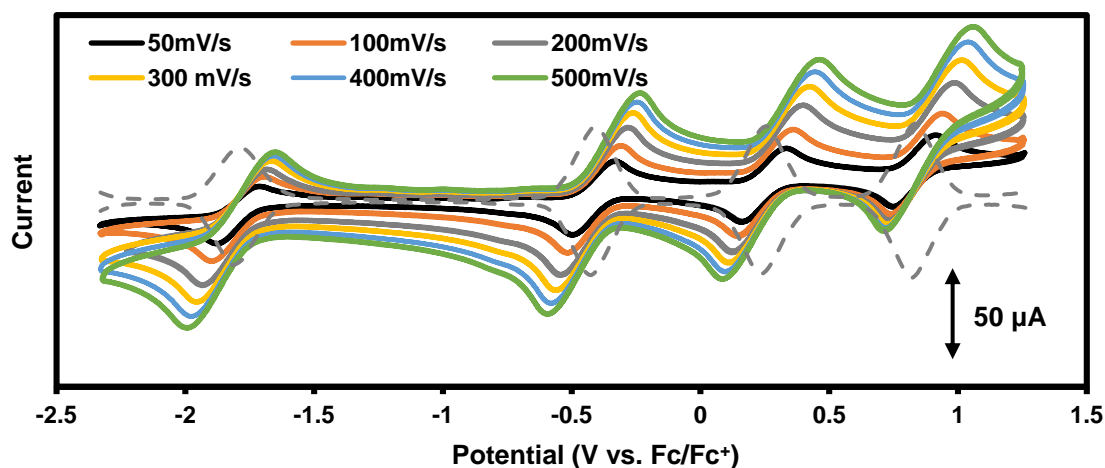


Figure 11. Cyclic voltammogram (solid traces) of $[\text{LFe}_3\text{F}(\text{PhPz})_3\text{Fe}(\text{NO})][\text{OTf}]$ (**1-NO**; 2 mM) in CH_2Cl_2 with 100 mM $[\text{Bu}_4\text{N}][\text{PF}_6]$ at various scan rates with glassy carbon, Pt-wire, and Ag-wire as working, reference, and counter electrode, respectively. Square wave voltammograms (gray dashed trace) overlaid with 0.1 V amplitude, 1.0 s period, and 0.01 V increment. The open circuit potential (OCP) was measured to be -0.7 V.

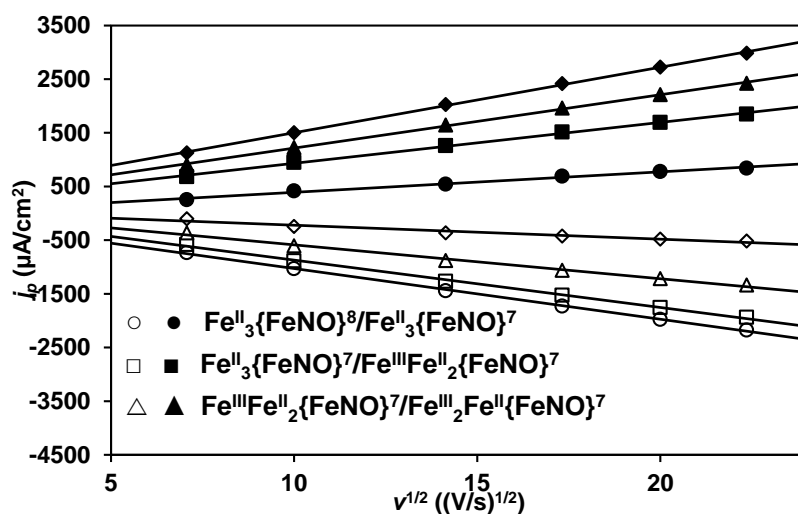


Figure 12. Current density (j_p) dependence of the square root of the scan rate $v^{1/2}$ for the electrochemical events observed in the CV of $[\text{LFe}_3\text{F}(\text{PhPz})_3\text{Fe}(\text{NO})][\text{OTf}]$, **1-NO**.

CRYSTALLOGRAPHIC DETAILS

Crystal and refinement data for complexes 1 – 3 and 1-NO – 3-NO.

	1	2	3	1-NO	2-NO	3-NO
CCDC Number	1554599	1554601	1554596	1554600	1554598	1554597
Empirical formula	C _{86.75} H ₆₂ Cl ₄ F ₄ Fe ₄ N ₁₂ O ₆ S	C ₉₆ H ₇₁ Cl ₂ F ₇ Fe ₄ N ₁₂ O ₉ S ₂	C _{101.5} H ₇₅ F ₁₀ Fe ₄ N ₁₄ O ₁₂ S ₃	C ₉₃ H ₇₆ Cl ₁₆ F ₄ Fe ₄ N ₁₃ O ₇ S	C ₉₃ H ₇₄ Cl ₁₄ F ₇ Fe ₄ N ₁₃ O ₁₀ S ₂	C _{89.92} H _{64.86} Cl ₅ . ₈₅ F ₁₀ Fe ₄ N ₁₃ O _{7.5} S ₅
Formula weight (g/mol)	1837.80	2028.06	2235.21	2386.32	2450.16	2252.38
Radiation	MoK α (λ = 0.71073)	MoK α (λ = 0.71073)	MoK α (λ = 0.71073)	CuK α (λ = 1.54178)	MoK α (λ = 0.71073)	CuK α (λ = 1.54178)
a (Å)	12.4213(18)	40.6924(19)	16.1006(6)	18.7000(7)	20.1692(15)	17.8680(9)
b (Å)	16.108(2)	17.6138(8)	16.1006(6)	16.8237(7)	17.4343(13)	20.4024(11)
c (Å)	20.502(3)	25.6670(13)	67.515(3)	32.4277(11)	28.440(2)	26.3282(15)
α (°)	78.323(6)	90	90	90	90	78.386(4)
β (°)	78.274(7)	114.015(2)	90	103.821(2)	99.091(2)	72.564(3)
γ (°)	85.537(6)	90	120	90	90	82.836(3)
V (Å ³)	3930.6(10)	16804.3(14)	15157.0(13)	9906.5(7)	9874.8(13)	8948.2(9)
Z	2	8	6	4	4	4
Cryst. syst.	triclinic	monoclinic	trigonal	monoclinic	monoclinic	triclinic
Space group	P-1	C2/c	R-3	P2 ₁ /n	P2 ₁ /n	P-1
ρ_{calc} (cm ⁻³)	1.553	1.603	1.469	1.600	1.648	1.672
2 Θ range (°)	2.584 to 61.034	4.626 to 55.754	5.060 to 61.146	5.004 to 130.168	4.464 to 51.356	9.042 to 179.202
μ (mm ⁻¹)	0.960	0.877	0.712	9.351	1.076	8.167
GOF	0.998	1.026	1.051	1.052	1.060	1.033
R1, wR2 (I > 2 σ (I))	0.0400, 0.1003	0.0458, 0.0959	0.0835, 0.2216	0.1232, 0.2937	0.0944, 0.2594	0.0786, 0.2045

Special refinement details for $[\text{LFe}_3\text{F}(\text{PhPz})_3\text{Fe}][\text{OTf}]$ (1). The structure contains several co-crystallized solvent molecules, many of which are on special positions. The only complete solvent molecule in the asymmetric unit that could be refined was disordered over two positions refined as 34.1% (C14 through C102) and 65.9% (C12 through C101). The two remaining solvent molecules were also disordered over two positions, but on a symmetry element. One disordered dichloromethane was refined as a partially occupied carbon 25% (C103) with $\sim 50\%$ occupied chlorine groups (Cl6 and Cl7). The other disordered dichloromethane was refined as a half occupied molecule, disordered over a symmetry element.

Special refinement details for $[\text{LFe}_3\text{F}(\text{PhPz})_3\text{Fe}][\text{OTf}]_2$ (2). This structure contains two triflate counterions, one of which is positionally disordered over two positions with refined occupancies of 78.5% (S201 through C201) and 21.5% (S202 through C202). The structure also contains a co-crystallized dichloromethane (C0AA through Cl20), and two benzene molecules; one is complete (C101 through C106) the other (C107 through C109) is on a special position. Rigid bond restraints were used on the triflate counterions.

Special refinement details for $[\text{LFe}_3\text{F}(\text{PhPz})_3\text{Fe}(\text{MeCN})][\text{OTf}]_3$ (3). This structure contains the cluster on a C_3 rotation axis, and therefore the three irons in the tri-iron core (Fe1 through Fe1^{''}) are indistinct. One triflate counterion is observed in the asymmetric unit along with four solvent molecules, only two of which could be modeled satisfactorily. A toluene molecule (C104 through C107) was disordered over a special position. There was another disordered toluene and acetonitrile that were disordered near special positions, based on residual electron density peaks; however, they could not be satisfactorily modeled. A solvent mask was used to account for the electron density of these molecules.

Special refinement details for $[\text{LFe}_3\text{F}(\text{PhPz})_3\text{Fe}(\text{NO})][\text{OTf}]$ (1-NO). This structure contained numerous co-crystallized solvent molecules (eight dichloromethane molecules). One solvent molecule was disordered and modeled with occupancies of 69% (C111 through C105) and 31% (C18 through C104). Another dichloromethane contained a disordered chlorine atom that was modeled with occupancies of 63% (C115) and 37% (C114). The triflate counterion was positionally disordered, whereby the sulfur would point either towards or away from the cluster. It was refined as two molecules with occupancies of 61% (S200 through C200) and 39% (S201 through C201). The standard deviations of some atoms in the phenyl ring of the trinucleating ligand (C34 – C36) were restrained to be the same.

Special refinement details for $[\text{LFe}_3\text{F}(\text{PhPz})_3\text{Fe}(\text{NO})][\text{OTf}]_2$ (2-NO). The structure contains two triflate counterions. One counterion is disordered over two positions with occupancies of 79.3% (S202 through C202) and 20.7% (S201 through C201). Three of the seven co-crystallized dichloromethane molecules are disordered over two positions. The first has occupancies of 59% (C111 through C105) and 41% (C103 through C108).

Special refinement details for $[\text{LFe}_3\text{F}(\text{PhPz})_3\text{Fe}(\text{NO})][\text{OTf}]_3$ (3-NO). There are two molecules in the asymmetric unit of the crystal structure. One of the clusters (Fe0A through C199) has a disordered phenyl pyrazolate ligand. Because of this disorder, the bond lengths and angles were not considered with in this molecule and only the other cluster, for which there was no evidence of disorder, (Fe1 through C99) was used for reporting bond metrics. All but two triflate counterions were disordered. Three triflates were positionally disordered; the first two had occupancies of 78% (S303 through C303 and S304 through C304) and 22% (S302 through C302 and S305 through C305). The third triflate had occupancies of 76% (S306 through C306) and 24% (S307 through C307). The two remaining triflates were disordered as a pair. They could be modeled as being adjacent to one another with occupancies of 51%

(S308 through C308) and 62% (S130 through C130). This would be disordered with two triflates, one occupying the same space as the first pair with an occupancy of 37% (S309 through C309), and the other, itself disordered, next to a symmetry element with an occupancy of 50%. There were seven dichloromethane solvent molecules modeled in the structure. Two had positionally disordered chlorine atoms with occupancies of 78% (Cl9) and 22% (Cl16), and 51% (Cl5) and 49% (Cl6). Another dichloromethane was only partially occupied (taking up the same space as the disordered pair of triflates, as discussed above); it had an occupancy of 36% (Cl10 through C205).

Selected bond angles and distances for complexes 1-3, 1-NO – 3-NO.

Bond Distance (Å)	Complex					
	1	2	3	1-NO	2-NO	3-NO
Fe1–F1	2.167(1)	2.024(1)	2.132(2)	2.129(7)	2.030(4)	2.207(3)
Fe2–F1	2.154(1)	2.204(1)	–	2.205(6)	2.237(4)	2.080(3)
Fe3–F1	2.174(1)	2.216(1)	–	2.169(5)	2.101(4)	2.091(3)
Fe4–F1	1.997(1)	2.011(1)	2.172(4)	2.065(7)	2.093(4)	2.155(3)
Fe1–N13	2.170(2)	2.076(2)	2.061(3)	2.118(10)	2.076(5)	2.057(4)
Fe2–N23	2.187(2)	2.125(2)	–	2.122(8)	2.102(5)	2.046(4)
Fe3–N33	2.157(2)	2.108(2)	–	2.116(11)	2.083(6)	2.025(4)
Fe4–N14	2.034(2)	2.063(2)	–	2.049(10)	2.064(6)	2.020(4)
Fe4–N24	2.056(2)	2.056(2)	–	2.060(9)	2.057(6)	2.049(4)
Fe4–N34	2.046(2)	2.044(2)	–	2.044(10)	2.064(5)	2.025(4)
N13–N14	1.390(2)	1.386(3)	1.387(5)	1.401(15)	1.389(7)	1.369(6)
N23–N24	1.383(2)	1.389(3)	–	1.398(13)	1.380(8)	1.371(6)
N33–N34	1.387(2)	1.388(3)	–	1.384(13)	1.379(8)	1.389(5)
Fe4–N40	–	–	2.112(8)	1.757(10)	1.773(6)	1.754(4)
N40–O40	–	–	–	1.163(13)	1.147(7)	1.133(6)
Bond Angles (°)						
N14–Fe4–N24	119.24(7)	119.34(8)	117.323	118.5(4)	114.6(2)	119.99(2)
N24–Fe4–N34	117.34(7)	120.91(8)	–	117.1(4)	119.8(2)	116.37(2)
N34–Fe4–N14	123.35(7)	119.26(8)	–	119.1(4)	119.6(2)	114.83(2)
Fe4–N40–O40	–	–	–	175.7(9)	177.0(6)	179.2(4)
Torsion Angles (°)						
Fe1–N13– N14–Fe4	3.640	3.40	27.095	23.02	29.86	23.320
Fe2–N23– N24–Fe4	1.317	4.02	–	31.89	30.26	23.035
Fe3–N33– N34–Fe4	4.968	2.14	–	30.32	22.64	25.985
Centroid Distances (Å)						
Fe1 Fe2 Fe3N 14 N24 N34	3.090	2.972	2.832	2.889	2.856	2.828
Fe1 Fe2Fe3– O11 O21 O31	0.974	0.945	1.008	0.959	0.987	0.926
Fe1 Fe2 Fe3– F1	1.093	1.051	0.975	1.100	1.063	1.029
N14 N24 N34 –Fe4	0.053	0.084	0.344	0.276	0.296	0.353

References

1. Bertini, I.; Gray, H. B.; Stiefel, E. I.; Valentine, J. S. *Biological Inorganic Chemistry: Structure and Reactivity*. 1st ed.; University Science Books: Sausalito, California, 2007.
2. (a) Peters, J. W.; Stowell, M. H. B.; Soltis, S. M.; Finnegan, M. G.; Johnson, M. K.; Rees, D. C. *Biochemistry* **1997**, *36*, 1181-1187; (b) Liu, J.; Chakraborty, S.; Hosseinzadeh, P.; Yu, Y.; Tian, S.; Petrik, I.; Bhagi, A.; Lu, Y. *Chem. Rev.* **2014**, *114*, 4366-4469; (c) Brown, K.; Djinojic-Carugo, K.; Haltia, T.; Cabrito, I.; Saraste, M.; Moura, J. G.; Moura, I.; Tegoni, M.; Cambillau, C. *J. Biol. Chem.* **2000**, *275*, 41133-41136; (d) Drennan, C. L.; Heo, J.; Sintchak, M. D.; Schreiter, E.; Ludden, P. W. *Proc. Natl. Acad. Sci.* **2001**, *98*, 11973-11978; (e) Dobbek, H.; Svetlitchnyi, V.; Gremer, L.; Huber, R.; Meyer, O. *Science* **2001**, *293*, 1281-1285.
3. (a) Ferreira, K. N.; Iverson, T. M.; Maghlaoui, K.; Barber, J.; Iwata, S. *Science* **2004**, *303*, 1831-1838; (b) Umena, Y.; Kawakami, K.; Shen, J.-R.; Kamiya, N. *Nature* **2011**, *473*, 55-60.
4. (a) Einsle, O.; Tezcan, F. A.; Andrade, S. L. A.; Schmid, B.; Yoshida, M.; Howard, J. B.; Rees, D. C. *Science* **2002**, *297*, 1696-1700; (b) Lancaster, K. M.; Roemelt, M.; Ettenhuber, P.; Hu, Y.; Ribbe, M. W.; Neese, F.; Bergmann, U.; DeBeer, S. *Science* **2011**, *334*, 974-977; (c) Spatzal, T.; Aksoyoglu, M.; Zhang, L.; Andrade, S. L. A.; Schleicher, E.; Weber, S.; Rees, D. C.; Einsle, O. *Science* **2011**, *334*, 940.
5. (a) Churchill, M. R.; Wormald, J. *J. Chem. Soc., Dalton Trans.* **1974**, 2410-2415; (b) Churchill, M. R.; Wormald, J.; Knight, J.; Mays, M. J. *J. Am. Chem. Soc.* **1971**, *93*, 3073-3074; (c) Kuppuswamy, S.; Wofford, J. D.; Joseph, C.; Xie, Z.-L.; Ali, A. K.; Lynch, V. M.; Lindahl, P. A.; Rose, M. J. *Inorg. Chem.* **2017**, *56*, 5998-6012; (d) Ćorić, I.; Holland, P. L. *J. Am. Chem. Soc.* **2016**, *138*, 7200-7211.
6. Taheri, A.; Berben, L. A. *Inorg. Chem.* **2016**, *55*, 378-385.
7. (a) Ohki, Y.; Ikagawa, Y.; Tatsumi, K. *J. Am. Chem. Soc.* **2007**, *129*, 10457-10465; (b) Ohta, S.; Ohki, Y.; Hashimoto, T.; Cramer, R. E.; Tatsumi, K. *Inorg. Chem.* **2012**, *51*, 11217-11219; (c) Chen, X.-D.; Duncan, J. S.; Verma, A. K.; Lee, S. C. *J. Am. Chem. Soc.* **2010**, *132*, 15884-15886; (d) Chen, X.-D.; Zhang, W.; Duncan, J. S.; Lee, S. C. *Inorg. Chem.* **2012**, *51*, 12891-12904; (e) Powers, T. M.; Betley, T. A. *J. Am. Chem. Soc.* **2013**, *135*, 12289-12296; (f) Fout, A. R.; Zhao, Q.; Xiao, D. J.; Betley, T. A. *J. Am. Chem. Soc.* **2011**, *133*, 16750-16753; (g) Cinco, R. M.; Rompel, A.; Visser, H.; Aromí, G.; Christou, G.; Sauer, K.; Klein, M. P.; Yachandra, V. K. *Inorg. Chem.* **1999**, *38*, 5988-5998; (h) Bobrik, M. A.; Laskowski, E. J.; Johnson, R. W.; Gillum, W. O.; Berg, J. M.; Hodgson, K. O.; Holm, R. H. *Inorg. Chem.* **1978**, *17*, 1402-1410; (i) Di Francesco, G. N.; Gaillard, A.; Ghiviriga, I.; Abboud, K. A.; Murray, L. J. *Inorg. Chem.* **2014**, *53*, 4647-4654.
8. de Ruiter, G.; Thompson, N. B.; Lionetti, D.; Agapie, T. *J. Am. Chem. Soc.* **2015**, *137*, 14094-14106.
9. (a) de Ruiter, G.; Thompson, N. B.; Takase, M. K.; Agapie, T. *J. Am. Chem. Soc.* **2016**, *138*, 1486-1489; (b) de Ruiter, G.; Carsch, K. M.; Gul, S.; Chatterjee, R.; Thompson, N. B.; Takase, M. K.; Yano, J.; Agapie, T. *Angew. Chem. Int. Ed.* **2017**, *56*, 4772-4776; (c) Han, Z.; Horak, K. T.; Lee, H. B.; Agapie, T. *J. Am. Chem. Soc.* **2017**, *139*, 9108-9111.
10. Tsui, E. Y.; Kanady, J. S.; Day, M. W.; Agapie, T. *Chem. Commun.* **2011**, *47*, 4189-4191.
11. McCleverty, J. A. *Chem. Rev.* **2004**, *104*, 403-418.
12. (a) Victor, E.; Lippard, S. J. *Inorg. Chem.* **2014**, *53*, 5311-5320; (b) Tran, C. T.; Williard, P. G.; Kim, E. *J. Am. Chem. Soc.* **2014**, *136*, 11874-11877; (c) Harrop, T. C.; Tonzetich, Z. J.; Reisner, E.; Lippard, S. J. *J. Am. Chem. Soc.* **2008**, *130*, 15602-15610.
13. (a) Majumdar, A.; Lippard, S. J. *Inorg. Chem.* **2013**, *52*, 13292-13294; (b) Awasabisah, D.; Xu, N.; Gautam, K. P. S.; Powell, D. R.; Shaw, M. J.; Richter-Addo, G. B. *Eur. J. Inorg. Chem.* **2016**, *2016*, 509-518; (c) Han, B.; Shao, J.; Ou, Z.; Phan, T. D.; Shen, J.; Bear, J. L.; Kadish, K. M. *Inorg. Chem.* **2004**, *43*, 7741-7751; (d) Victor, E.; Minier, M. A.; Lippard, S. J. *Eur. J. Inorg. Chem.* **2014**, *2014*, 5640-5645; (e) Sidebotham, R. P.; Beer, P. D.; Hamor, T. A.; Jones, C. J.; McCleverty, J. A. *J. Organomet. Chem.* **1989**, *371*, C31-C34.
14. Herbert, D. E.; Lionetti, D.; Rittle, J.; Agapie, T. *J. Am. Chem. Soc.* **2013**, *135*, 19075-19078.
15. Enemark, J. H.; Feltham, R. D. *Coord. Chem. Rev.* **1974**, *13*, 339-406.
16. Shannon, R. *Acta Crystallographica Section A* **1976**, *32*, 751-767.

17. (a) Martirosyan, G. G.; Kurtikyan, T. S.; Azizyan, A. S.; Iretskii, A. V.; Ford, P. C. *J. Inorg. Biochem.* **2013**, *121*, 129-133; (b) Praneeth, V. K. K.; Näther, C.; Peters, G.; Lehnert, N. *Inorg. Chem.* **2006**, *45*, 2795-2811; (c) Wyllie, G. R. A.; Schulz, C. E.; Scheidt, W. R. *Inorg. Chem.* **2003**, *42*, 5722-5734; (d) Sharma, S. K.; Kim, H.; Rogler, P. J.; A. Siegler, M.; Karlin, K. D. *JBIC Journal of Biological Inorganic Chemistry* **2016**, *21*, 729-743.
18. (a) Creutz, S. E.; Peters, J. C. *J. Am. Chem. Soc.* **2014**, *136*, 1105-1115; (b) Rittle, J.; Peters, J. C. *Proc. Natl. Acad. Sci.* **2013**, *110*, 15898-15903; (c) Cammarota, R. C.; Clouston, L. J.; Lu, C. C. *Coord. Chem. Rev.* **2017**, *334*, 100-111.
19. (a) Schoenberg, A. R.; Anderson, W. P. *Inorg. Chem.* **1972**, *11*, 85-87; (b) Hallett, A. J.; Angharad Baber, R.; Guy Orpen, A.; Ward, B. D. *Dalton Transactions* **2011**, *40*, 9276-9283; (c) Imai, S.; Fujisawa, K.; Kobayashi, T.; Shirasawa, N.; Fujii, H.; Yoshimura, T.; Kitajima, N.; Moro-oka, Y. *Inorg. Chem.* **1998**, *37*, 3066-3070; (d) Kujime, M.; Kurahashi, T.; Tomura, M.; Fujii, H. *Inorg. Chem.* **2007**, *46*, 541-551; (e) Thomas, J. C.; Peters, J. C. *J. Am. Chem. Soc.* **2003**, *125*, 8870-8888; (f) Thomas, J. C.; Peters, J. C. *Inorg. Chem.* **2003**, *42*, 5055-5073.
20. (a) Speelman, A. L.; Lehnert, N. *Angew. Chem. Int. Ed.* **2013**, *52*, 12283-12287; (b) Speelman, A. L.; Zhang, B.; Krebs, C.; Lehnert, N. *Angew. Chem. Int. Ed.* **2016**, *55*, 6685-6688.
21. (a) Sanders, B. C.; Patra, A. K.; Harrop, T. C. *J. Inorg. Biochem.* **2013**, *118*, 115-127; (b) Kupper, C.; Rees, J. A.; Dechert, S.; DeBeer, S.; Meyer, F. J. *J. Am. Chem. Soc.* **2016**, *138*, 7888-7898.
22. Taheri, A.; Thompson, E. J.; Fettingner, J. C.; Berben, L. A. *ACS Catalysis* **2015**, *5*, 7140-7151.
23. Rauchfuss, T. B. Bio-Inspired Iron and Nickel Complexes. In *Inorg. Synth.*, John Wiley & Sons, Inc.: 2010; pp 129-147.
24. Izod, K.; Rayner, D. G.; El-Hamruni, S. M.; Harrington, R. W.; Baisch, U. *Angew. Chem. Int. Ed.* **2014**, *53*, 3636-3640.
25. (a) Larina, N. A.; Lokshin, V.; Berthet, J.; Delbaere, S.; Vermeersch, G.; Khodorkovsky, V. *Tetrahedron* **2010**, *66*, 8291-8299; (b) Kiss, L.; David, L.; Da Costa Pereira Rosa, C. P.; De Nornha, R. G.; Palma, P. N. L.; Da Silva, A. S.; Beliaev, A. US Patent 2012/65191, Mar 15, 2012.
26. Sun, H.; DiMugno, S. G. *J. Am. Chem. Soc.* **2005**, *127*, 2050-2051.
27. Yueh, W.; Bauld, N. L. *J. Am. Chem. Soc.* **1995**, *117*, 5671-5676.
28. Barton, D. H. R.; Haynes, R. K.; Leclerc, G.; Magnus, P. D.; Menzies, I. D. *J. Chem. Soc., Perkin Trans. 1* **1975**, 2055-2065.
29. (a) Herold, S.; Lippard, S. J. *Inorg. Chem.* **1997**, *36*, 50-58; (b) Singh, A. K.; Jacob, W.; Boudalis, A. K.; Tuchagues, J.-P.; Mukherjee, R. *Eur. J. Inorg. Chem.* **2008**, *2008*, 2820-2829; (c) Sutradhar, M.; Carrella, L. M.; Rentschler, E. *Eur. J. Inorg. Chem.* **2012**, *2012*, 4273-4278; (d) Schünemann, V.; Hauke, P. Mössbauer Spectroscopy. In *Applications of Physical Methods to Inorganic and Bioinorganic Chemistry*, Scott, R. A.; Lukehart, C. M., Eds. John Wiley & Sons: West Sussex, England, 2007; pp 243-269.